



**HAL**  
open science

## Radiation Patterns Control the Near-Source Ground-Motion Saturation Effect

Alain Dujardin, Mathieu Causse, Catherine Berge-thierry, Fabrice Hollender

► **To cite this version:**

Alain Dujardin, Mathieu Causse, Catherine Berge-thierry, Fabrice Hollender. Radiation Patterns Control the Near-Source Ground-Motion Saturation Effect. Bulletin of the Seismological Society of America, 2018, 108 (6), pp.3398-3412. 10.1785/0120180076 . cea-02430310

**HAL Id: cea-02430310**

**<https://cea.hal.science/cea-02430310>**

Submitted on 7 Jan 2020

**HAL** is a multi-disciplinary open access archive for the deposit and dissemination of scientific research documents, whether they are published or not. The documents may come from teaching and research institutions in France or abroad, or from public or private research centers.

L'archive ouverte pluridisciplinaire **HAL**, est destinée au dépôt et à la diffusion de documents scientifiques de niveau recherche, publiés ou non, émanant des établissements d'enseignement et de recherche français ou étrangers, des laboratoires publics ou privés.

## Abstract

We investigate the feasibility of near-fault ground-motion predictions based on empirical Green's functions (EGFs) in low-to-moderate seismicity areas (i.e., with few available EGFs), and we propose some adjustments to enhance the accuracy of this method. We conduct extended fault ground-motion simulations for a large set of azimuths, based on a kinematic model description according to the  $k^{-2}$  method combined with the use of numerical Green's functions. We focus on saturation of the ground-motion peak values observed in near-field data for moderate-to-large earthquakes, and we seek to identify the physical mechanisms behind this phenomenon. Based on the simulation performed here for a specific magnitude and focal mechanism, we show that the radiation pattern has a major influence on the near-source ground-motion saturation effect, and that the saturation effect can be seen more strongly for some azimuths compared to others, due to the orientation of the source. We also show that the depth of the source has a role, as it defines the radiation pattern. Finally, we show that unlike previously thought, geometric and anelastic attenuation adjustments are weak, as are the time-shift adjustments due travel-time differences from the different parts of the fault, and these do not account for the near-fault saturation effect.

## Introduction

In moderate seismicity regions, seismic hazard assessment relies on a small amount of available data. In these regions, such as the metropolitan French territory, records of moderate to large earthquakes often do not exist, let alone near-fields recordings of such events. Ground motion estimation is then performed through the use of Ground Motion Prediction Equations (GMPEs) established from data recorded in other regions or numerical simulations.

One fundamental feature of moderate to large earthquakes is the finite fault dimensions which induces a saturation of the ground motion peak values in the near field (e.g. [Yenier & Atkinson, 2014](#)). Using a pure point-source model, ground motion amplitudes continue to increase as the recording station is closer to the fault. Conversely, real observations and finite-fault ground motion modeling show that as one gets sufficiently close to the source, the observed ground motion amplitude saturates (it stops growing). This effect especially depends on the fault size, and is then magnitude dependent: the saturation extends to larger distances with increasing magnitude.

Thanks to the increasing number of strong motion observations and the improving quality of data and metadata, this phenomenon is now accounted for in GMPEs through the functional forms used for regression (see [Fukushima et al. \(2003\)](#) and [Zhao et al., \(2006\)](#) for example). It can also be mimicked in point source simulations through the use of an effective distance ([Atkinson & Silva, 2000](#); [Boore, 2015](#)). The effective distance represents an estimation of the average distance between the station and all fault points, where fault dimensions are estimated empirically ([Yenier & Atkinson, 2014](#); [Boore & Thompson, 2015](#)).

However, very few studies have attempted to identify the physical mechanisms behind the saturation effect. It is however the major influence on the ground motion peak values near the source (up to 25 km for a  $M$  5.0 event, and up to 35 km for a  $M$  6.0 event, see [Dujardin et al., 2015](#)). [Rogers & Perkins \(1996\)](#) highlight the role of isochrones (i.e. loci on the rupture area for which the radiated energy arrives at a given station at the same time), whose length increases with fault size, both on magnitude dependence of the ground motion decay and the finite fault saturation effect. [Anderson \(2000\)](#) highlights the role of constructive interferences between the different parts of the rupture area. These interferences increase as the distance increases, partly because of the decrease of arrival time's differences between the different parts of the fault. Both of these assumptions support the idea that the closest portions of the rupture of large earthquakes dominate the motions recorded close to the fault. As such, the  $R_{RUP}$  (used in this study) and  $R_{JB}$  definitions of the source-to-site distance are a priori more adapted for extended fault at short distance than distance definitions based on a point-source model such as  $R_{EPI}$  and  $R_{HYP}$ .  $R_{JB}$  and  $R_{RUP}$  represent the closest distance between the site and the projection of the rupture area, and between the site and the rupture area, respectively;  $R_{EPI}$  and  $R_{HYP}$  represent the distance between the site and the projection of the nucleation point and between the site and the nucleation point respectively. For example, the [Boore et al. \(2014\)](#) GMPE uses the  $R_{JB}$  definition, but this is not the case in most of the commonly used GMPEs. Thus, the choice of a suitable distance definition is crucial in the GMPEs implementation because it controls the strong motions predictions at short distances ([Sherbaum et al., 2004](#)).

When the use of GMPEs is not possible to perform seismic hazard analyses (e.g. when ground motion time series are required or for site specific studies), simulations techniques must be deployed. One relevant simulation approach is the summation of small magnitude events, used as empirical Green functions (EGF) ([Hartzell, 1978](#)), which implicitly accounts for the complexity of propagation and site effects in a broad frequency range (e.g. [Causse et al., 2009](#); [Dujardin et al., 2016](#)). In low to moderate seismicity areas, this approach remains however difficult to deploy for near-fault ground motion predictions because of the limited number of events that can be used as EGF. Several selection criteria further limit the number of available small events (limited range of magnitude, position, focal mechanism, see [Dujardin et al. 2016](#) for details). When simulations are performed with a limited number of EGFs and in near-source area, the distances between the different parts of the fault and the target station strongly vary. Some EGF adjustments are then necessary to properly account for directivity effects, geometrical spreading and variations of the radiation pattern, among other effects.

The objective of this study is to investigate the feasibility of near-fault EGF-based ground motion predictions in low-to-moderate seismicity areas (that is, with few available EGFs) and propose some adjustments to enhance the method accuracy. In particular, we investigate the conditions under which the saturation effect is properly modeled. Our analysis is conducted using numerical ground motion simulations based on finite-fault source models. The source is described according to the  $k^{-2}$  method ([Bernard et al., 1996](#); [Causse et al., 2009](#)). The method enables to derive static slip distributions, which allow generating a variable set of source time functions that respect the  $\omega^{-2}$  model ([Aki, 1967](#); [Brune, 1970](#)). The Green's functions are numerically computed using the wave number method, assuming a 1D-layered visco-elastic medium ([Bouchon, 1981](#); [Coutant, 1989](#)). Green's functions can then be computed for any pair of fault point and surface receiver of the assumed 1D medium, so as to analyze the ground motion uncertainty induced by a spatially sparse set of Green's functions.

The simulations are first performed for an ideal case (referenced later as the “ideal case”), in which 45 numerical Green’s functions distributed over the entire rupture area are used. This “ideal case” is then degraded, so as to mimic a sparser set of available Greens functions and investigate the influence of various effects (geometrical spreading, anelastic attenuation, variation of the radiation pattern) on the saturation effects. The simulated ground motion peaks values are also compared with a point-source stochastic simulations, which account for the finite fault saturation effect through the use of a finite fault factor (FFF) described in [Boore & Thompson \(2015\)](#). Finally additional simulations are carried out to study the impact of the depth of the considered set of Green’s functions.

## I Method (K2)

### I.1. Static slip distribution

This code has been developed to perform ground motion simulations of a hypothetical future event. In such as case, there is no available recording and the physical characteristics of the source are unknown, except the seismic moment  $M_0$  and the focal mechanism which are postulated. The rupture area dimensions are then calculated automatically from the stress drop value and  $M_0$ . The stress drop is chosen to be a free entry parameter, to be constrained by the user, for several reasons. First, although the stress drop has been considered as constant since the fundamental work of [Aki \(1967\)](#), it may vary from one region to another ([Chouet et al., 1978](#)). Secondly, the variability of the stress drop values is significant with variations generally ranging between 0.1 and 100 MPa ([Allmann & Shearer, 2009](#)). Moreover, this similar hypothesis is now questioned and it is suggested that the constant stress drop condition is not appropriate for a large scale of magnitude ([Beeler et al., 2003](#), [Kanamori & Rivera, 2004](#), [Drouet et al., 2011](#)).

The dimensions of the rupture area are derived as follow: from the stress drop ( $\Delta\sigma$ ), we derive the corner frequency ( $f_c$ ) following [Boore \(2003\)](#):

$$f_c = \left( \frac{16 \Delta\sigma}{7 M_0} \right)^{1/3} k \beta_S \quad (1)$$

with  $\beta_S$  the S wave (m/s) velocity and  $M_0$  the seismic moment (Nm) and the stress drop is in Pa.

This allows deriving the rupture duration ( $T_{RUP}$ ), according to the following approximation ([Hanks, 1979](#); [Hanks & McGuire, 1981](#)):

$$f_c = \frac{1}{T_{RUP}} \quad (2)$$

And then, we can estimate the dimensions of the rupture area thanks to the expression:

$$T_{RUP} = \frac{\sqrt{L^2 + W^2}}{V_R} \quad (3)$$

where  $V_R$  represents the average rupture velocity and  $L$  and  $W$  are the length and the width of the fault respectively. Thus only the ratio between  $L$  and  $W$  is necessary to derive the dimensions of the

rupture area. The  $V_R$  value depends on the velocity of the S waves ( $V_S$ ) in the vicinity of the fault, and commonly varies between  $0.7$  and  $0.85 \cdot V_S$  (Heaton, 1990). The S wave velocity in the vicinity of the fault is also used to derive the differences in travel time between the different parts of the rupture area to a station. Both  $V_S$  and the ratio between  $V_S$  and  $V_R$  are parameters to be constrained by the user.

The last parameter to be constrained is purely numerical. It is the spatial sampling of the slip distribution on the rupture area (i.e. the size of each subfault). Indeed, the  $k^{-2}$  theory allows to constrain the spectrum to simulate only up to the Nyquist wavenumber ( $k_{NY}$ ). This one depends on the sampling rate in the spatial domain ( $k_{ech}$ ) of the rupture area, or on the size of each subfault ( $SF_{dim}$ ):

$$k_{NY} = \frac{k_{ech}}{2} = \frac{1}{2 \cdot SF_{dim}} \quad (4)$$

Beyond this limit, we observe the phenomenon of spatial aliasing. This has the consequence of limiting the spectrum in the frequency domain to the maximum frequency  $f_{kmax}$  :

$$f_{kmax} = k_{NY} \cdot V_R \quad (5)$$

Thus, by fixing the target frequency limit ( $f_{kmax}$ ), the fault size can be defined by combining equations 5 and 6 :

$$SF_{dim} = \frac{V_R}{2 \cdot f_{kmax}} \quad (6)$$

Once the rupture area dimensions are defined, the low and the high frequency part of the slip distribution are constrained separately. The low frequency part is defined homogeneously over the whole rupture area at the value of the mean slip. This mean slip  $\bar{D}$  is derived from the relation between the seismic moment and the rupture area dimensions:

$$M_0 = \mu S \bar{D} \quad (7)$$

where  $S=L \cdot W$  is the rupture area, and  $\mu = \rho V_S^2$ . We use a density  $\rho=2.7\text{g/cm}^3$  and  $V_S$  is the S wave velocity.

The high frequency complexity of the static slip distribution is defined for any wavenumber greater than  $\sqrt{\left(\frac{1}{L}\right)^2 + \left(\frac{1}{W}\right)^2}$ . It is described according to Herrero & Bernard (1994) in order to have an asymptotic decay in  $k^{-2}$  in the wavenumber domain, beyond the corner wavenumber  $k_C$ . By analogy, the source model in  $\omega^{-2}$  (Brune, 1970) exhibit an  $\omega^{-2}$  decay beyond the corner frequency  $f_C$ . Since the fault plane is rectangular, the amplitude spectrum is defined similarly to Somerville et al. (1999) and Galovic & Brokesova (2003) :

$$Dk(k_x, k_y) = \frac{\bar{D}LW}{\sqrt{1 + \left[ \left(\frac{k_x}{k_{Cx}}\right)^2 + \left(\frac{k_y}{k_{Cy}}\right)^2 \right]^2}} \quad (8)$$

where  $k_x$  and  $k_y$  represent respectively the wavenumber in the strike and the dip directions (direction of the length and the width).

The corner wavenumber associated to the strike and the dip direction are defined as  $k_{c_x} = k_c \frac{W}{L}$  and  $k_{c_y} = k_c \frac{L}{W}$ . In such a way that  $\sqrt{k_{c_x} * k_{c_y}} = k_c$ , with  $k_c$  the corner wavenumber which will define the corner frequency of the simulated event.

By analogy with the relation which connects the corner frequency  $f_c$  with the rupture duration  $T_{RUP}$  (equation 2), the corner wavenumber can be expressed as a function of the characteristic rupture dimension denoted  $D_{RUP}$  :

$$k_c = \frac{1}{D_{RUP}} \quad (9)$$

where  $D_{RUP} = T_{RUP} * V_R$ . This allows us to derive the expression of  $k_c$ :

$$k_c = \frac{f_c}{V_R} \quad (10)$$

The high frequency spectrum phases are defined in a purely random way. Then the high frequency contributions of the slip are obtained by the inversion of the total high frequency spectrum (composed of the amplitude and the phase spectra). Finally the final static slip map is obtained by summing the high and the low frequencies parts.

## 1.2. Rupture kinematics and absolute source time function

The theoretical  $k^{-2}$  source model of [Bernard et al. \(1996\)](#) allows to generate source time function which respect the empirical  $\omega^{-2}$  model under the following conditions: (1) the wavenumber slip distribution spectrum falls as the inverse of the wavenumber squared ( $k^{-2}$ ), (2) the Fourier amplitudes of the slip velocity are independent of  $\omega$  at high frequencies, and (3) the rupture velocity is constant.

In this study we choose to follow the approach by [Hisada \(2000\)](#) who proposes a more realistic model by introducing rupture velocity variations. According to this approach, the last two conditions cited above are modified. First the slip velocity is defined by the model of [Kostrov, \(1964\)](#) by superimposing triangles, and a variable rupture velocity is introduced. This rupture velocity variation is modeled in two dimensions, through a rupture time variation, over the entire rupture area according to a  $k^{-2}$  model, which is recognized as the most plausible one among those tested by [Hisada \(2001\)](#):  $k^{-1}$ ,  $k^{-2}$  and  $k^{-3}$ . Thus, the rupture time of the subfault whose position (i,j) is given by:

$$T_{ij} = \frac{D_{nuc}(i,j)}{V_R} * (1 + \Delta T_R(i,j)) \quad (11)$$

where  $D_{nuc}(i,j)$  is the distance between the nucleation point of the rupture, and the subfault of position (i,j).  $V_R$  is the average rupture velocity and  $\Delta T_R(i,j)$  the rupture time variation, (expressed as a percentage) at the (i,j) position.

Following the [Hisada \(2001\)](#) formulation, the amplitude spectrum of the rupture time variation on the rupture area is given by :

$$\Delta T k(k_x, k_y) = \frac{1}{\sqrt{1 + \left[ \left( \frac{k_x}{kcT_x} \right)^2 + \left( \frac{k_y}{kcT_y} \right)^2 \right]}} \quad (12)$$

where  $kcT_x$  et  $kcT_y$  are the corner wavenumbers in the direction of the strike (along length) and the dip (along width) respectively. These parameters make it possible to control the characteristic dimensions of the rupture time perturbations  $Dim_{\Delta T_R}^X$  and  $Dim_{\Delta T_R}^Y$  in the strike and dip directions, respectively:

$$Dim_{\Delta T_R}^{(X,Y)} = \frac{1}{kcT_{(x,y)}} \quad (13)$$

Each of these dimensions is fixed independently, randomly for each simulation, in an interval chosen by the user, proportional to the length and the width of the rupture area. As for the slip spectrum, the phase spectrum of the velocity perturbation is defined randomly. Finally, the rupture time perturbation map is obtained by inverse Fourier transform, and normalized so as not to exceed the percentage of the rupture velocity chosen by the user.

The rupture propagates from the nucleation point, whose position is fixed by the user. The slip rate function on each subfault  $SRF_{ij}$  is defined according to the approach proposed by [Hisada \(2000\)](#) as a sum of triangular functions. The slip duration (i.e. the rise time  $\tau_{rise}$ ) is constant over the fault plane and constrained according to the [Somerville et al., \(1999\)](#) regressions :

$$\tau_{rise} = 2.03 \times 10^{-9} (M_0)^{1/3} \quad (15)$$

where  $M_0$  is in dyne.cm.

The absolute source time function is then obtained by summing each subfault contribution:

$$R_{abs}(t) = \sum_{i=1}^{NL} \sum_{j=1}^{NW} [\delta(t - T_{ij}) S_{ij} * SRF_{ij}] \quad (16)$$

where  $NL$  et  $NW$  are the subfault numbers in the strike and the dip direction respectively,  $S_{ij}$  represent the values of the static slip, and  $SRF_{ij}$  is the slip rate function for the subfault  $(i,j)$ .

### I.3. Time series generation and Green's functions corrections

The simulated displacement  $U(\vec{r}, t)$  at position  $\vec{r}$ , is expressed numerically according to the discrete representation theorem ([Aki & Richard, 2002](#)) :

$$U(\vec{r}, t) = \sum_{i=1}^{NL} \sum_{j=1}^{NW} [R_{ij} * FG_{ij}(\vec{r}, t)] \quad (17)$$

where  $R_{ij}$  represents the contribution of subfault  $(i,j)$  to the absolute source time function ([equation 16](#)) and  $FG_{ij}(\vec{r}, t)$  is the Green's function associated to the same subfault. As mentioned above, in real applications of the EGF technique, the set of Green's functions  $FG_{ij}(\vec{r}, t)$  is approximated using a limited number of small earthquake recordings. In case of a unique available Green's function (called  $FG_0(\vec{r}, t)$ ), several adjustments may be applied, described in the following.

The first adjustment consists in shifting  $FG_0(\vec{r}, t)$  by a time  $\Delta t(i,j)$ , so as to incorporate the directivity effect of the rupture propagation. The  $\Delta t(i,j)$  values are defined as follows:

$$\Delta t(i,j) = \frac{R_{STA(\vec{r})}^{SFij} - R_{STA(\vec{r})}^{FG_0}}{V_s} \quad (18)$$

where  $R_{STA(\vec{r})}^{SFij}$  represents the distance between the subfault (i,j) and the station at the position  $\vec{r}$  considered and  $R_{STA(\vec{r})}^{FG_0}$  the distance between the Green's function and the station at the position  $\vec{r}$ . The adjusted Green function is then expressed as:

$$FG_{ij}^{adj,1} = \delta(t - \Delta t(i,j))FG_0(\vec{r}, t) \quad (19)$$

The second adjustment concerns the geometrical attenuation term. The distances between each subfault and the station ( $R_{STA(\vec{r})}^{SFij}$ ) being different, the geometrical attenuation difference (in  $1/R$ ) is taken into account by the correction of the Green's function amplitude:

$$FG_{ij}^{adj,2} = FG_{ij}^{adj,1} \times \frac{R_{STA(\vec{r})}^{FG_0}}{R_{STA(\vec{r})}^{SFij}} \quad (20)$$

with  $R_{STA(\vec{r})}^{FG_0}$  the true distance between the Green's function used and the station, and  $R_{STA(\vec{r})}^{SFij}$  the distance between the subfault of position (i,j) and the station.

The third correction concerns the anelastic attenuation, still applied for the same distance difference than before. The anelastic attenuation, modelised by the quality factor  $Q(f)$ , is frequency dependent. Then this correction is applied in the frequency domain:

$$FG_{ij}^{adj,3} = iFFT \left( FFT(FG_{ij}^{adj,2}) \cdot \exp \frac{-\pi f (R_{STA(\vec{r})}^{SFij} - R_{STA(\vec{r})}^{FG_0})}{Q_s f^\alpha} \right) \quad (21)$$

with  $Q(f) = Q_s f^\alpha$  the quality factor estimation for S wave, and  $f$  the frequency vector.

Finally, due to the inherent complexity of the wave radiation patterns, the amount of energy radiated toward a target strongly depends on the subfault position. In case of a single available Green's function some additional adjustments are then required. Such a correction is however not easy to implement since body waves are a complex combination of the near-field, intermediate and far-field of P and S waves, all associated with different radiation patterns (equation 21, from Aki & Richard, 2002). Since the proposed tests are purely numerical, this influence will be tested by the use of several Green's functions generated over the entire rupture area instead of using the unique Green's function  $FG_0(\vec{r}, t)$ .

In order to highlight the impact of each of these effects, we perform ground motion simulations considering various approximations of equation 17. The first case is the most complete (referenced as the ideal case) and take into account all the listed adjustments. This ideal case is then degraded,

by removing one by one the different adjustments proposed, so as to judge their relative influence. We consider the following 4 cases:

- Ideal case: this case represents the most realistic case and takes into account all the effects mentioned above. The set of Green's functions  $FG(\vec{r}, t)$  is represented by 45 Green's functions spread over the fault plane (Figure 5) so as to take into account the complexity of the radiation pattern. The number of subfaults being greater than 45, each Green's function is corrected, for the subfaults set on which it will be use, in the same way as the adjustments described in the case of a single Green's function (equation 19 to 21).
- No time shift case: we remove the time shift adjustment due to the travel time difference, which is at the origin of the directivity effect. The 45 numerical Green's functions are thus corrected so that their arrival time are all the same. In this way, we are able to judge the importance of the directivity effect alone.
- No radiation pattern case: the influence of the radiation pattern complexity is removed by replacing the set of 45 Green's functions by the use of a unique Green's function  $FG_0(\vec{r}, t)$ , located at the center of the fault plane (Figure 5), on the whole rupture area. This Green's function is still corrected from the geometric and anelastic attenuation when it is shifted from its original position, and not corrected from the time shift adjustment.
- No correction case: we remove the last adjustments (i.e. the geometric and anelastic attenuation adjustment, equation 20 and 21). This last case consists in the convolution of the absolute source function (same at every distance and azimuth) with the unique and uncorrected Green's function spread over the whole fault and is therefore comparable to a point source simulation.

## II Experiment description

We choose to generate a **M** 6.0 event (i.e.  $M_0=1.1220.10^{18} Nm$ ), which is a typical target in a seismic risk analysis for the metropolitan French territory, corresponding roughly to the maximal observed magnitude in instrumental database (e.g. the Lambesc 1909 earthquake whose magnitude is estimated at 6, Baroux et al., 2003). The S wave velocity of the propagation medium is fixed at  $V_S=3600$  m/s. The rupture velocity is defined at the fixed value of  $V_R=0.7*V_S=2520$  m/s (consistent with Heaton, 1990). The stress drop is defined at the fixed value of  $\Delta\sigma = 1.0$  MPa (consistent with Allman & Shearer, 2009). The corner frequency is then derived from the parameters listed above ( $M_0$ ,  $V_S$  and  $\Delta\sigma$ ) thanks to the equation 1, giving  $f_c=0.17$ Hz. By fixing a ratio of 1.6 between the length and the width of the rupture area, its dimensions are derived thanks to the equations 2 and 3:  $L=12650$ m and  $W=7900$ m. In order to be able to generate broadband simulations up to about 50 Hz, the fault is divided into sub-faults with dimensions  $SF_{dim} = 25$ m (equation 6).

We generate a population of 20 random static slip distributions (Figure 1) using the  $k^2$  model (equation 8). This population combined with the rupture kinematics results in a set of 20 rupture models which are used to compute synthetics at all the considered stations. According to the model proposed by Hisada (2001), rupture time perturbations are defined according to a  $k^2$  model

(equation 12). Since we are primarily interested on how the finite fault dimension influences the saturation of the ground motion peak values in the near field, we consider a smooth spatial variation of the rupture time. Then we have chosen to vary the characteristic dimensions of the rupture time variations between 30 and 70% of the L and W dimensions of the fault plane (equation 13), with rupture time variation values normalized so as not to exceed 10% (equation 11, Figure 2a). In this way we avoid to have too rude propagation front while maintaining a smooth variability (Figure 2b). The nucleation point is located at the bottom of the fault (consistent with Mai et al., 2005), at distances of  $0.15 \cdot L$  along the strike direction and  $0.8 \cdot W$  along the dip direction (Figure 2b). The generated absolute source functions exhibit a significant variability in the time domain (Figure 3a), but closely follow the  $\omega^{-2}$  model in the frequency domain (Aki, 1967; Brune, 1970) as imposed by the Hisada (2001) method (Figure 3b).

The fault is defined as a plane with a strike of  $0^\circ$  and a dip of  $60^\circ$ , and extends between 1.6 km and 8.4 km depth. The center of the rupture area is located at a depth of 5 km. The stations are placed all around the fault plane, every  $22.5^\circ$  of azimuth (from  $0^\circ$  to  $337.5^\circ$  N), with respect to the fault center. In each of these azimuths, stations are located at distances of 3, 6, 10, 20, 40 and 70 km from the projection of the rupture area at the surface (i.e. from a distance  $R_{JB}=0$  km). This leads to 96 stations, located at 16 different azimuths and 6 different distances (Figure 4).

The Green functions are numerically computed using the discrete wavenumber method (Bouchon, 1981), thanks to the development of Coutant (1989) modified so as to consider a frequency dependent quality factor. The 45 Green's functions used for the ideal case are distributed over the entire rupture area (every 1.5 km along-strike and along-dip, Figure 5). Their focal mechanisms are defined as strike, dip and rake values of  $0^\circ$ ,  $60^\circ$  and  $0^\circ$  respectively. The unique Green's function  $FG_0(\vec{r}, t)$  used for the last two simulation cases (no radiation pattern and no correction cases) is positioned at the center of the rupture area, at a depth of 5km (Figure 5).

We assume that the propagation medium is homogeneous half space, where  $V_p=5000m/s$  and  $V_s=3600m/s$  and the anelastic attenuation, defined through the quality factor is fixed at  $Q_p=50f^{0.2}$  for P-waves and  $Q_s=200f^{0.3}$  for S waves.

Finally we extract the peak values in acceleration (PGA) and velocity (PGV) from the generated synthetics. Those results are also compared with point-source stochastic simulations, incorporating saturation effect through the use of an effective distance (Atkinson & Silva, 2000). The stochastic simulations are generated according to the same parametrization as the one used in  $k^{-2}$  simulations: a **M** 6.0 event, a stress drop of 1.0 MPa, and an hypocentral distance equal to distance between the fault center and the station so as to facilitate the comparison with the no correction case. As for  $k^{-2}$  simulations, we generate a set of 20 stochastic simulations per stations. The duration of each of the 20 simulations is imposed as equal to the duration measured on each  $k^{-2}$  simulation. Two cases are considered for the stochastic simulations. The first one does not consider the saturation effect, whereas the second case uses an effective distance calculated based on the Boore & Thompson (2015) finite fault factor (FFF). We choose to fix the parameter which defines the energy distribution due to the radiation pattern at 1 (see equation 7 in Boore, 2003). In order to be consistent with the definition of geometric mean of the peak values, we also set to 1 the parameter of energy partition between the two horizontal components to 1 (see equation 7 in Boore, 2003).

### III Results

The stations being positioned along azimuths ranging from 0 to 360°, the energy will be distributed differently on the horizontal components depending on the station's azimuth. Therefore the peak values are computed as the geometric mean of the horizontal components. This choice is also motivated by the comparison with stochastic simulations which do not allow to generate a vertical component, nor to distinguish between the two horizontal components. Furthermore the peak values are averaged over the 20 rupture realizations. The PGA and PGV are presented as function of the rupture distance ( $R_{RUP}$ ) (Figure 6 and 7, respectively).

First, we observe that simulations in the “ideal case” exhibit a saturation effect. As described by Yenier & Atkinson (2014), as one get sufficiently close to the fault, the peak values cease to increase. This observation is valid for both PGA and PGV for all azimuth range (Figure 6 and 7).

The second observation pertains the directivity effect. The rupture propagates preferentially to the North, but has also a westward component (see the nucleation position, Figure 2). The suppression of the time shift adjustment as defined in equation 19 (i.e. “no time shift case”) has the effect to remove the directivity effect. Then by comparing the “no time shift case” and the “ideal case” we observe an amplification of the PGA and the PGV values due to the directivity effect at azimuth N0° and N22.5° and from azimuth N270° to N337.5° (Figure 6 and 7). Conversely, the anti-directivity effect tends to decrease the peak values, but this phenomenon is less visible (see azimuths N90° to N180°). Note that the suppression of the time shift correction does not seem to have a significant influence on the saturation effect.

Next we remove the influence of the radiation pattern complexity by the use of a unique Green's function summed over the entire fault plane (i.e. “no radiation pattern case”). While the unique Green's function is shifted from its original position, the anelastic and geometric attenuation adjustments are applied (equations 20 and 21), but we do not include any correction of the focal mechanism. The suppression of the radiation pattern influence leads to two observations. First, there is a sharp decrease in peak values in the nodal planes (Figure 8: “no radiation pattern case” compared with the “no time shift case”) of the unique Green's function (see azimuths N45°, N135°, N225°, N247.5°, 292.5° and N315° in Figure 6. It is observed at all distances, but this effect is stronger at the lowest distances. On the contrary, for all the other azimuths, we observe an increase of the peak values between the PGA of the “no time shift case” and the “no radiation pattern case” reaching 2 for the closest stations. These observations are also made for PGV (Figure 5) although the influence is less pronounced.

In the last case, the influence of the geometrical spreading and the anelastic attenuation is suppressed, and no correction is applied to the unique Green's function (i.e. “no correction case”). By comparing the “no radiation pattern case” and the “no correction case”, we can conclude that the difference of attenuation due to the geometrical extension of the fault has a negligible impact for all azimuths (Figure 6 and 7).

Ground motions computed using the  $k^2$  source model in the 4 cases analyzed above all exhibit a saturation effect. This means that a significant part of the saturation effect is not accounted for by any of the proposed adjustments, but is implicitly included in the “no correction case”. The “no correction case” is equivalent to a point source simulation because a single Green's function (not

corrected) is convolved with the absolute source time function to obtain ground motion. The comparison between the “no correction case” and the stochastic point source simulations performed without finite-fault factor (the one which do not incorporate saturation effects) clearly points out a ground motion saturation at short distance (Figures 6 and 7). In addition the “no correction case” and the stochastic simulations provides similar PGA and PGV attenuation curves at some azimuths if considering saturation in the stochastic simulation through the Boore & Thompson (2015) finite fault factor (referred to as BT15 FFF) (see in particular azimuths N00°, N180.0°, N202.5 and N337.5° in Figure 6). As explained in the following, the saturation effect observed in the no correction case is attributed to the depth of the Green’s function  $FG_0(\vec{r}, t)$ .

We then carry out additional simulations to investigate the sensitivity of the PGA and PGV attenuation curves to the depth of the Green’s function  $FG_0(\vec{r}, t)$ . Three simulation cases are considered: one with the Green’s function located at the top of the fault, one with the Green’s function at the center of the fault plane (“no correction case”) and one with the Green’s function at the base of the fault plane (see positions on Figure 5).

The results show a clear dependence, in the West direction (azimuth N270°), of the saturation effect to the depth of the Green’s function used: the deeper is the source, the more pronounced the saturation effect is. This observation is true for PGA and PGV (Figure 9 and 10).

We associate the saturation phenomenon observed to the vertical rotation around the radiation pattern as the station is getting closer to the epicenter. Indeed, for close stations, the ray path is much more vertical as the source location is depth, station is then in a weaker azimuth of the radiation pattern (see the west propagating ray paths, Figure 11). The same phenomenon can also be observed for the east direction, but it will appear for even smaller distances because of the orientation of the source (see the east propagating ray paths, Figure 11).

This last observation helps to explain that the saturation phenomenon observed in our  $k^{-2}$  simulations is stronger in the east direction (see azimuths N202.5° to N315° compared with azimuths N22.5° to NN135°, Figure 6 and 7). This difference is all the more important since it is visually amplified by the use of the  $R_{RUP}$  distance definition. For stations located at the same  $R_{JB}$  distance around the fault, the  $R_{RUP}$  distance will indeed be lower in the west direction than the others due to the west dip of the fault.

## Conclusion

The realization of reliable ground motion simulation represents a major issue in seismic hazard assessment to overcome the lack of data, especially at distances which can be affected by the saturation effect. The observation that ground motion ceases to increase as we get closer to the source is known as the saturation effect (Yenier & Atkinson, 2014). This effect is known and empirically taken into account in the GMPEs, but also in the point source numerical simulations. Very few studies have attempted to identify the physical mechanisms behind this phenomenon. However a good understanding of this phenomenon should allow a better consideration of it and a better consideration of the ground motion variability at distances closed to the source.

The work of [Roger & Perkins, \(1996\)](#) and [Anderson, \(2000\)](#) are both consistent with the commonly accepted hypothesis that this effect is due to the geometrical extension of the fault. But, if only the geometrical extension of the fault was at the origin of this phenomenon, the geometric and anelastic attenuation adjustments should be sufficient to reproduce the majority of this phenomenon. However, we note in our simulations that these two influences are weak.

In point source numerical simulations, [Atkinson & Silva \(2000\)](#) introduce the notion of effective distance. This distance is the one used in simulations, instead of the true hypocentral distance, in order to reproduce the geometrical extension of the fault. The effective distance is derived from a magnitude dependent parameter denominated by “pseudo depth”. This parameter is then reused by [Yenier & Atkinson \(2014\)](#) who use the denomination “saturation term” and by [Boore & Thompson \(2015\)](#) who call it “finite fault factor”. Our simulations showed that most of the saturation effect was reproduced by the no correction case (similar to a point source simulation). Our additional simulations highlight the role of the source depth, and more precisely the role of the vertical rotation of the station around the radiation pattern as this one is getting closer to the epicenter. That is why, we will prefer the original term of “pseudo depth” proposed by [Atkinson & Silva \(2000\)](#) to those proposed by [Yenier & Atkinson \(2014\)](#) and [Boore & Thompson \(2015\)](#). Moreover, the use of an effective distance does not make it possible to highlight the azimuthal variability of the ground motion at such distances.

In general way, the radiation pattern is the major influence on the ground motion amplitude, and on the saturation effect. The radiation pattern is indeed the major parameter that constrains the azimuthal ground motion variability, but also allows explaining a part of the saturation effect. Its orientation makes it possible to explain that this phenomenon is seen in some azimuths more than in others. The influence of the depth can also be brought back to the focal mechanism since the modification of the depth modifies the way we see the focal mechanism from the surface, thus modifying the strength of the saturation phenomenon.

In the context of extended fault simulation using a limited number of empirical Green’s functions, the radiation pattern correction on the whole rupture area represents the one that has the greatest impact on ground motion amplitude at short distances. Not taking this effect into account also exposes us to overestimations at short distances, and to strong misestimations near the nodal plane of the Green’s functions used. The dependence of the nearby stations ground motion, to the depth and the source orientation, also point to the importance of having quality metadata even on small magnitude seismic events.

## References

- Aki, K. (1967). Scaling law of seismic spectrum. *Journal of Geophysical Research*, 72(4), 1217-1231.
- Aki, K., & Richards, P. G. (2002). *Quantitative seismology*.
- Allmann, B. P., & Shearer, P. M. (2009). Global variations of stress drop for moderate to large earthquakes. *Journal of Geophysical Research: Solid Earth*, 114(B1).
- Anderson, J. G. (2000). Expected shape of regressions for ground-motion parameters on rock. *Bulletin of the seismological Society of America*, 90(6B), S43-S52.
- Atkinson, G. M., & Silva, W. (2000). Stochastic modeling of California ground motions. *Bulletin of the Seismological Society of America*, 90(2), 255-274.
- Baroux, E., Alessandro Pino, N., Valensise, G., Scotti, O. & Cushing, E. (2003). Source parameters of the June 11, 1909 Lambesc (Provence, southern France) earthquake: a reappraisal based on macroseismic and geodesic observations, *J. Geophys. Res.*, 108 (139).
- Beeler, N. M., Wong, T. F., & Hickman, S. H. (2003). On the expected relationships among apparent stress, static stress drop, effective shear fracture energy, and efficiency. *Bulletin of the Seismological Society of America*, 93(3), 1381-1389.
- Bernard, P., Herrero, A., & Berge, C. (1996). Modeling directivity of heterogeneous earthquake ruptures. *Bulletin of the Seismological Society of America*, 86(4), 1149-1160.
- Boore, D. M. (2003). Simulation of ground motion using the stochastic method. In *Seismic Motion, Lithospheric Structures, Earthquake and Volcanic Sources: The Keiiti Aki Volume* (pp. 635-676). Birkhäuser Basel.
- Boore, D. M., Stewart, J. P., Seyhan, E., & Atkinson, G. M. (2014). NGA-West2 equations for predicting PGA, PGV, and 5% damped PSA for shallow crustal earthquakes. *Earthquake Spectra*, 30(3), 1057-1085.
- Boore, D. M., & Thompson, E. M. (2015). Revisions to some parameters used in stochastic-method simulations of ground motion. *Bulletin of the Seismological Society of America*.
- Bouchon, M. (1981). A simple method to calculate Green's functions for elastic layered media. *Bulletin of the Seismological Society of America*, 71(4), 959-971.
- Brune, J. N. (1970). Tectonic stress and the spectra of seismic shear waves from earthquakes. *Journal of geophysical research*, 75(26), 4997-5009.
- Causse, M., Chaljub, E., Cotton, F., Cornou, C., & Bard, P. Y. (2009). New approach for coupling  $k-2$  and empirical Green's functions: application to the blind prediction of broad-band ground motion in the Grenoble basin. *Geophysical Journal International*, 179(3), 1627-1644.
- Chouet, B., Aki, K., & Tsujiura, M. (1978). Regional variation of the scaling law of earthquake source spectra. *Bulletin of the Seismological Society of America*, 68(1), 49-79.
- Coutant, O. (1989). Program of numerical simulation AXITRA. *Res. Rep. LGIT (in French), Université Joseph Fourier, Grenoble*.

- Drouet, S., Bouin, M. P., & Cotton, F. (2011). New moment magnitude scale, evidence of stress drop magnitude scaling and stochastic ground motion model for the French West Indies. *Geophysical Journal International*, 187(3), 1625-1644.
- Dujardin, A., Courboux, F., Causse, M., & Traversa, P. (2015). Influence of Source, Path, and Site Effects on the Magnitude Dependence of Ground-Motion Decay with Distance. *Seismological Research Letters*.
- Dujardin, A., Causse, M., Courboux, F., & Traversa, P. (2016). Simulation of the Basin Effects in the Po Plain During the Emilia-Romagna Seismic Sequence (2012) Using Empirical Green's Functions. *Pure and Applied Geophysics*, 173(6), 1993-2010.
- Fukushima, Y., Berge-Thierry, C., Volant, P., Griot-Pommeroy, D. A., & Cotton, F. (2003). Attenuation relation for West Eurasia determined with recent near-fault records from California, Japan and Turkey. *Journal of Earthquake Engineering*, 7(04), 573-598.
- Galovič, F., & Brokešová, J. (2003). On strong ground motion synthesis with  $k=2$  slip distributions. *Journal of Seismology*, 8(2), 211-224.
- Hanks, T. C. (1979).  $b$  values and  $\omega-\gamma$  seismic source models: Implications for tectonic stress variations along active crustal fault zones and the estimation of high-frequency strong ground motion. *Journal of Geophysical Research: Solid Earth*, 84(B5), 2235-2242.
- Hanks, T. C., & McGuire, R. K. (1981). The character of high-frequency strong ground motion. *Bulletin of the Seismological Society of America*, 71(6), 2071-2095.
- Hartzell, S. H. (1978). Earthquake aftershocks as Green's functions. *Geophysical Research Letters*, 5(1), 1-4.
- Heaton, T. H. (1990). Evidence for and implications of self-healing pulses of slip in earthquake rupture. *Physics of the Earth and Planetary Interiors*, 64(1), 1-20.
- Herrero, A., & Bernard, P. (1994). A kinematic self-similar rupture process for earthquakes. *Bulletin of the Seismological Society of America*, 84(4), 1216-1228.
- Hisada, Y. (2000). A theoretical omega-square model considering the spatial variation in slip and rupture velocity. *Bulletin of the Seismological Society of America*, 90(2), 387-400.
- Hisada, Y. (2001). A theoretical omega-square model considering spatial variation in slip and rupture velocity. Part 2: Case for a two-dimensional source model. *Bulletin of the Seismological Society of America*, 91(4), 651-666.
- Kanamori, H., & Rivera, L. (2004). Static and dynamic scaling relations for earthquakes and their implications for rupture speed and stress drop. *Bulletin of the Seismological Society of America*, 94(1), 314-319.
- Kostrov, B. V. (1964). Selfsimilar problems of propagation of shear cracks. *Journal of Applied Mathematics and Mechanics*, 28(5), 1077-1087.
- Mai, P. M., Spudich, P., & Boatwright, J. (2005). Hypocenter locations in finite-source rupture models. *Bulletin of the Seismological Society of America*, 95(3), 965-980.
- Rogers, A. M., & Perkins, D. M. (1996). Monte Carlo simulation of peak-acceleration attenuation using a finite-fault uniform-patch model including isochrone and extremal characteristics. *Bulletin of the Seismological Society of America*, 86(1A), 79-92.

- Scherbaum, F., Schmedes, J., & Cotton, F. (2004). On the conversion of source-to-site distance measures for extended earthquake source models. *Bulletin of the Seismological Society of America*, 94(3), 1053-1069.
- Somerville, P., Irikura, K., Graves, R., Sawada, S., Wald, D., Abrahamson, N., ... & Kowada, A. (1999). Characterizing crustal earthquake slip models for the prediction of strong ground motion. *Seismological Research Letters*, 70(1), 59-80.
- Yenier, E., & Atkinson, G. M. (2014). Equivalent point-source modeling of moderate-to-large magnitude earthquakes and associated ground-motion saturation effects. *Bulletin of the Seismological Society of America*.
- Zhao, J. X., Zhang, J., Asano, A., Ohno, Y., Oouchi, T., Takahashi, T., ... & Fukushima, Y. (2006). Attenuation relations of strong ground motion in Japan using site classification based on predominant period. *Bulletin of the Seismological Society of America*, 96(3), 898-913.

## FIGURES

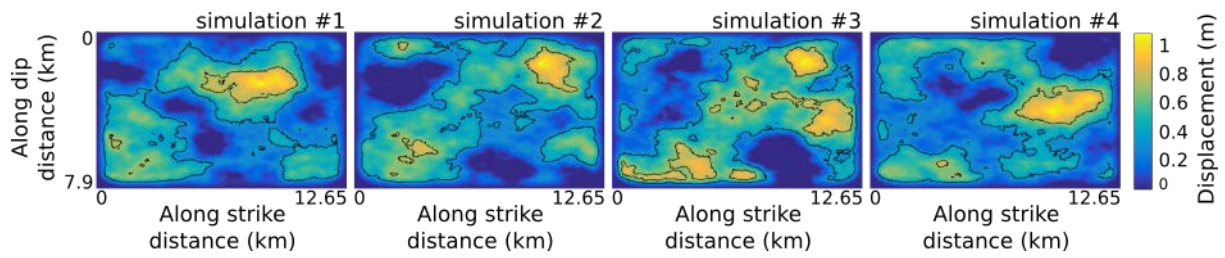


Figure 1: Realization of static slip distributions over the rupture area, generated from the  $k^2$  source model.

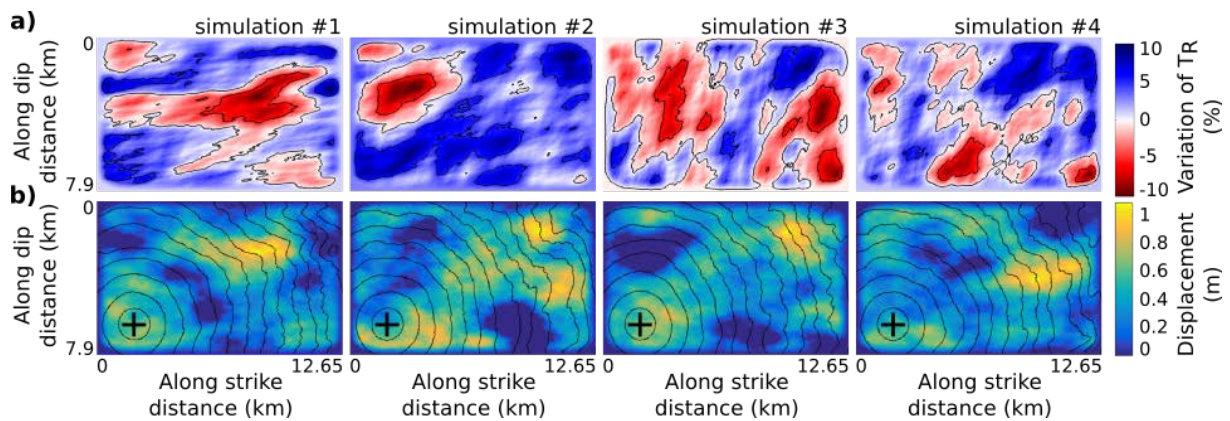


Figure 2: a) Examples of distribution of the rupture time perturbations over the rupture area expressed as a percentage of the rupture time  $T_r$  computed for the average velocity (according to the  $k^2$  source model of Hisada, 2001). The characteristic dimensions of the perturbation are  $0.7 \cdot L \times 0.4 \cdot W$  for simulation #1,  $0.6 \cdot L \times 0.6 \cdot W$  for simulation #2,  $0.3 \cdot L \times 0.7 \cdot W$  for simulation #3 and  $0.3 \cdot L \times 0.6 \cdot W$  for simulation #4. b) Representation of the rupture front propagation. Isolines of the rupture time are represented every  $1/15$  of the total propagation time. The nucleation position is represented by a black cross.

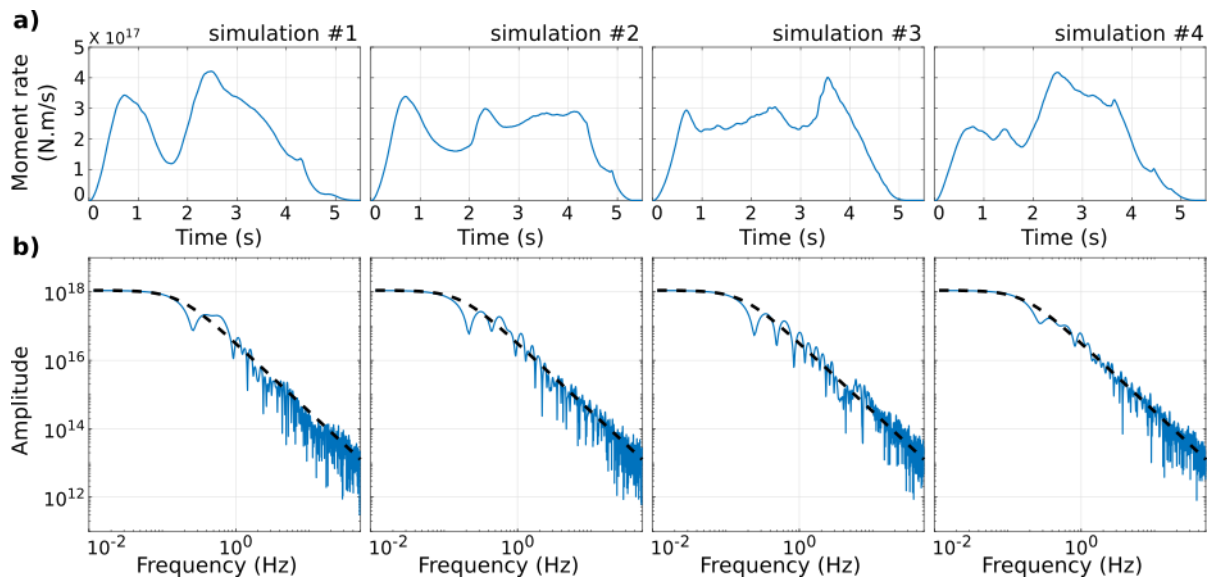


Figure 3: a) Realization of absolute source time functions generated by the  $k^{-2}$  method (Hisada, 2001). b) The spectra of these absolute source time functions are compared with the  $\omega^{-2}$  reference model (black dashed line).

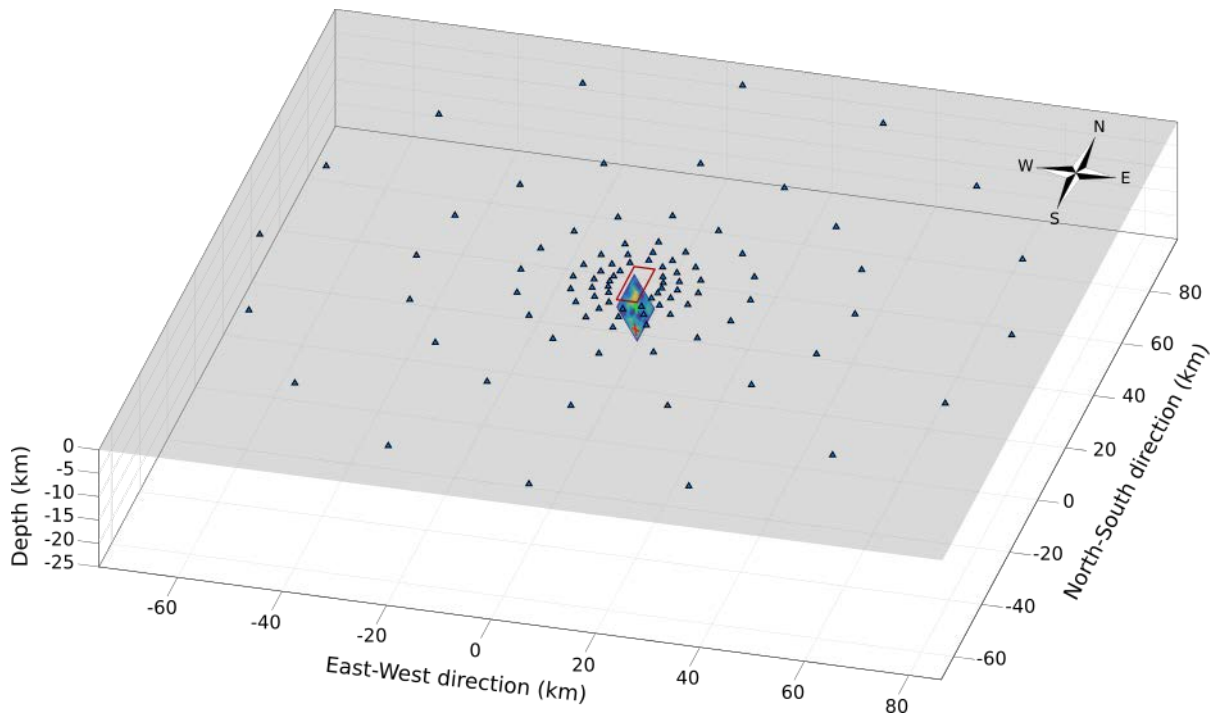


Figure 4: General representation of the experiment geometry. The rupture area is represented in the center, and its surface projection is shown in red. Stations in the 16 azimuths are represented by blue triangles.

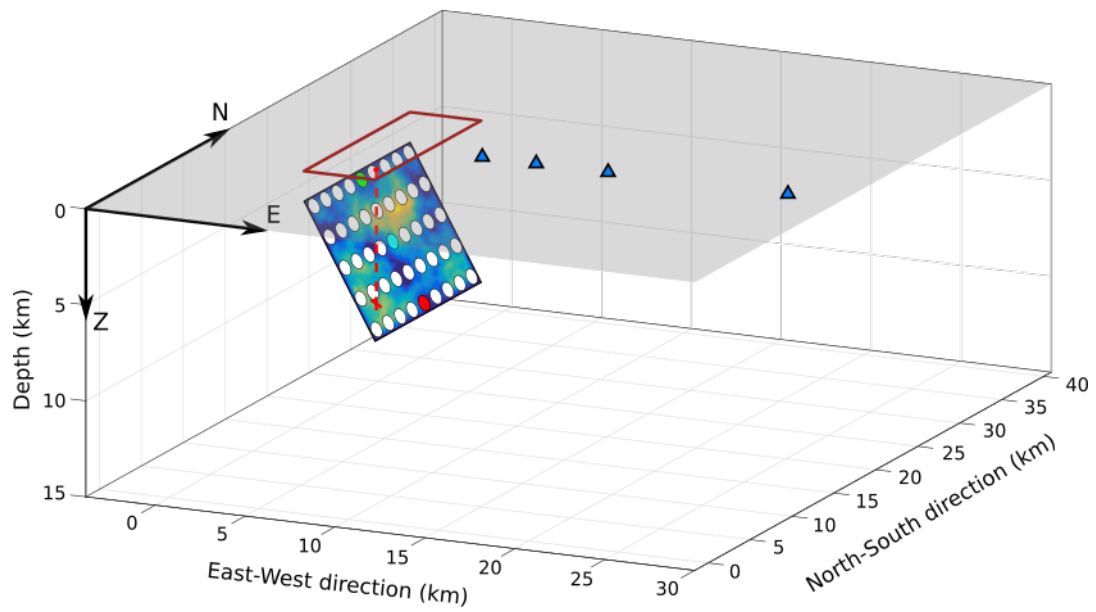


Figure 5: Representation of the fault geometry, its surface projection (in red), and the first four stations along the azimuth  $90^\circ\text{N}$ . The positions of the 45 Green's functions distributed over the whole rupture area and used to compute ground motion in the ideal case and the no time shift case are represented by white dots. The unique Green's function  $FG_0(\vec{r}, t)$ , used for the other cases is located at the center of the fault plane and represented by a blue dot. The two positions of the Green's functions used in the additional simulation case are represented by a green and a red dot at the top and the bottom of the fault plane respectively. The position of the rupture nucleation is indicated by a red cross.

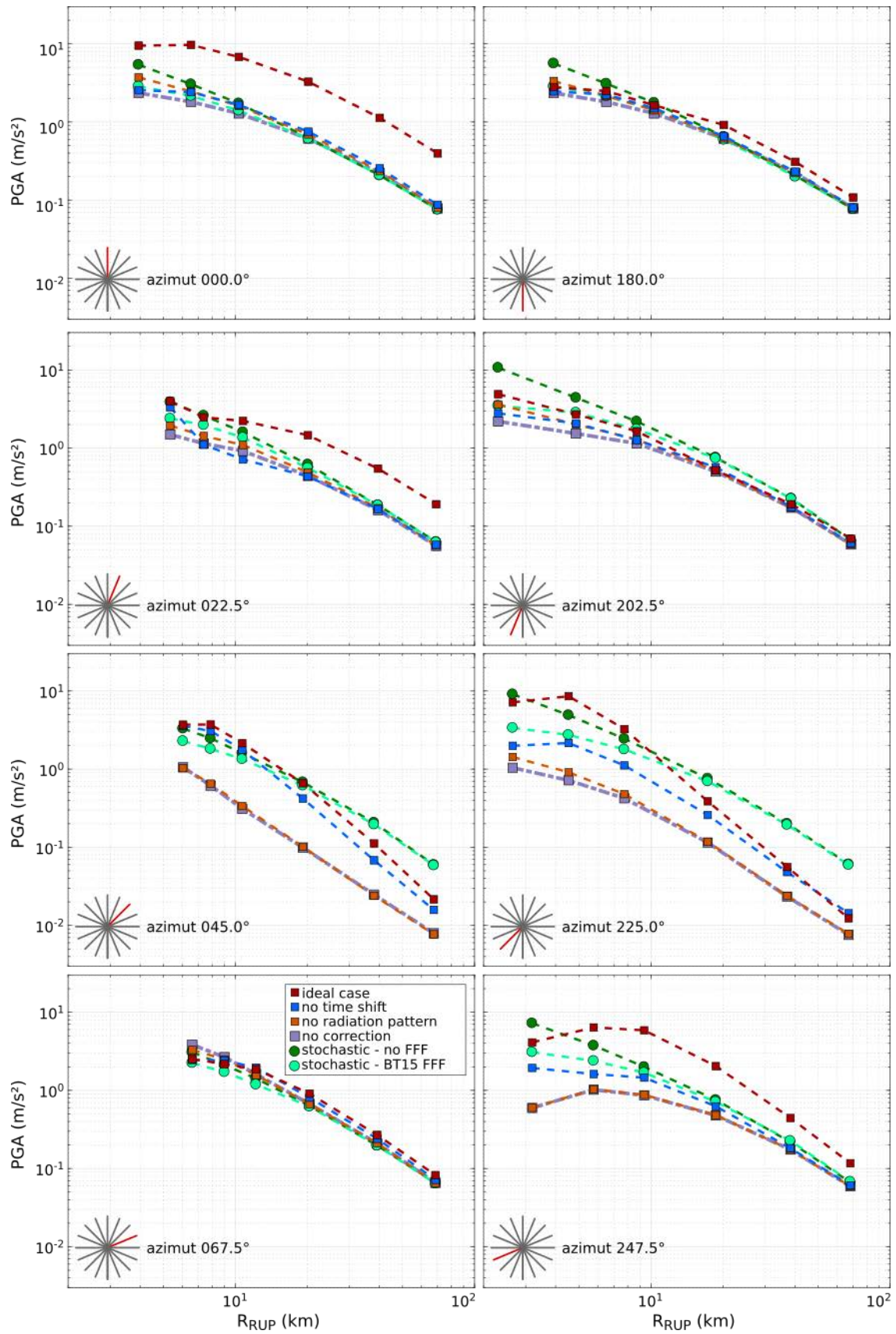


Figure 6: Comparison between the peak ground acceleration values (PGA) calculated for the different cases described in section 1.3. The PGA is calculated as the geometric mean of the two horizontal

components. Each point represents the average value of 20 realizations of rupture scenarios. The azimuths range from 0° to 67.5°N (left), and from 180° to 247.5°N (right).

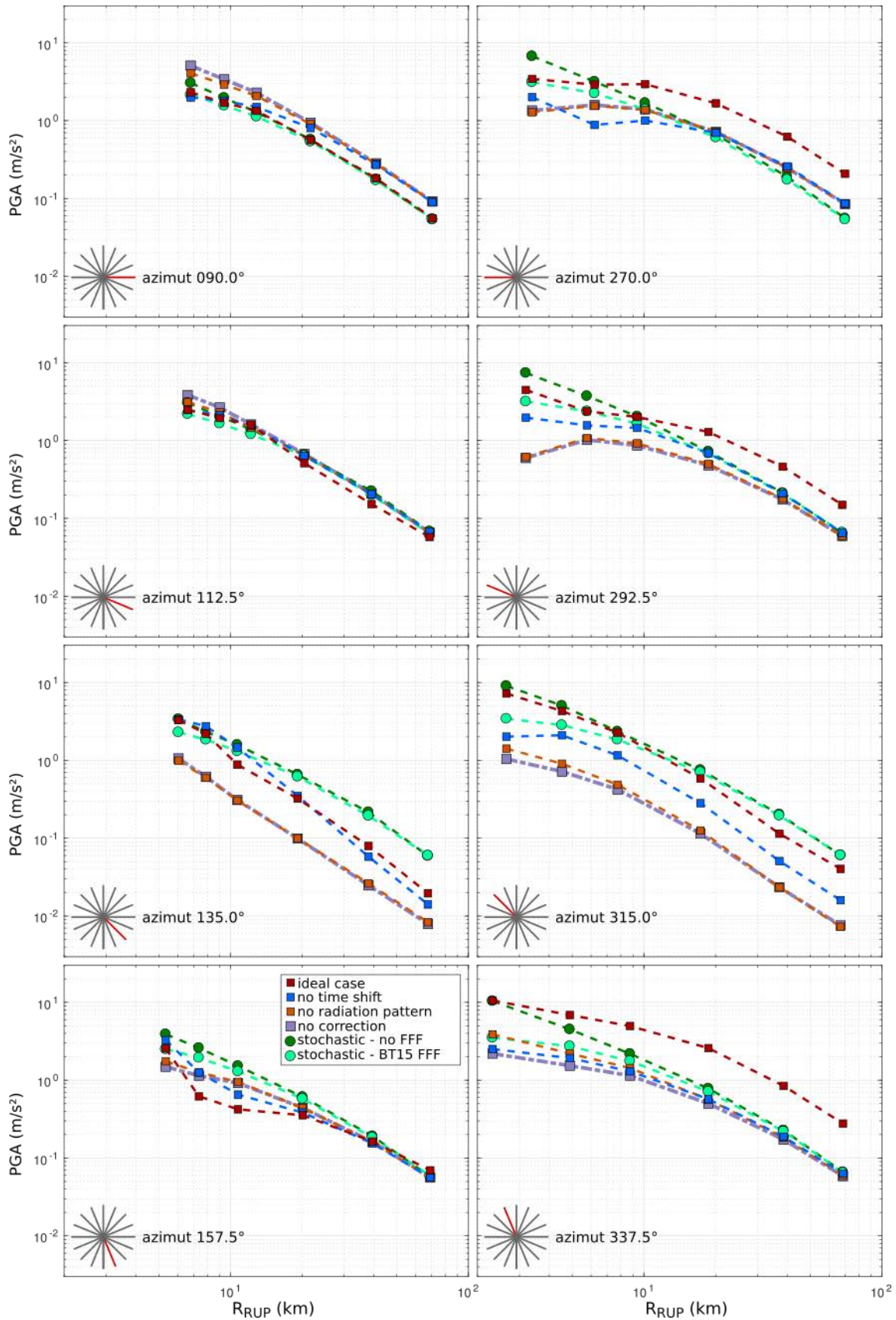


Figure 6 (continued) : Azimuths from 90° to 157.5°N (left) and 270° to 337.5°N (right).

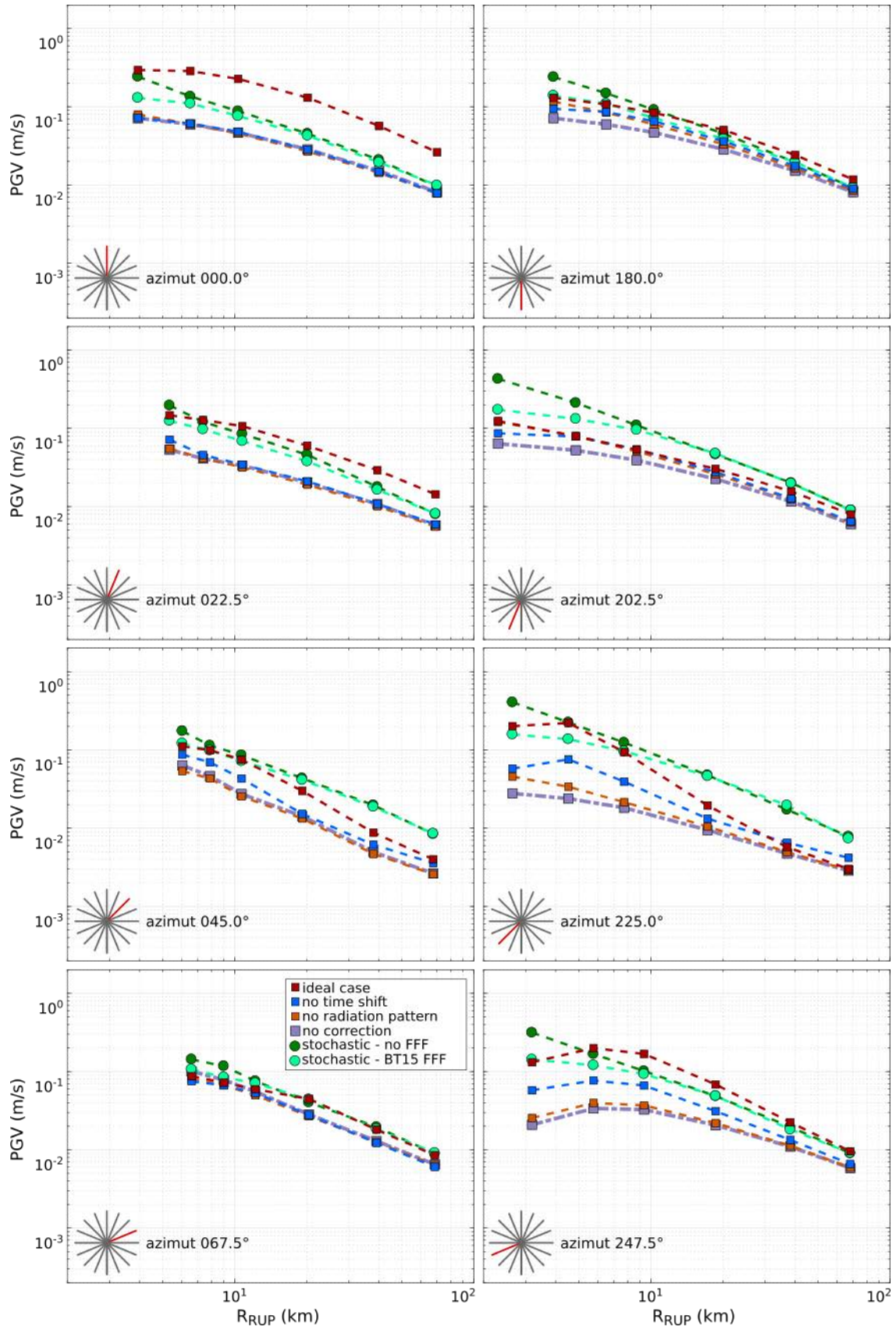


Figure 7 : Comparison between the peak ground velocity values (PGV) calculated for the different cases described in section 1.3. The PGA is calculated as the geometric mean of the two horizontal

components. Each point represents the average value of 20 realizations of rupture scenarios. The azimuths range from  $0^\circ$  to  $67.5^\circ$  (left) and from  $180^\circ$  to  $247.5^\circ$  (right).

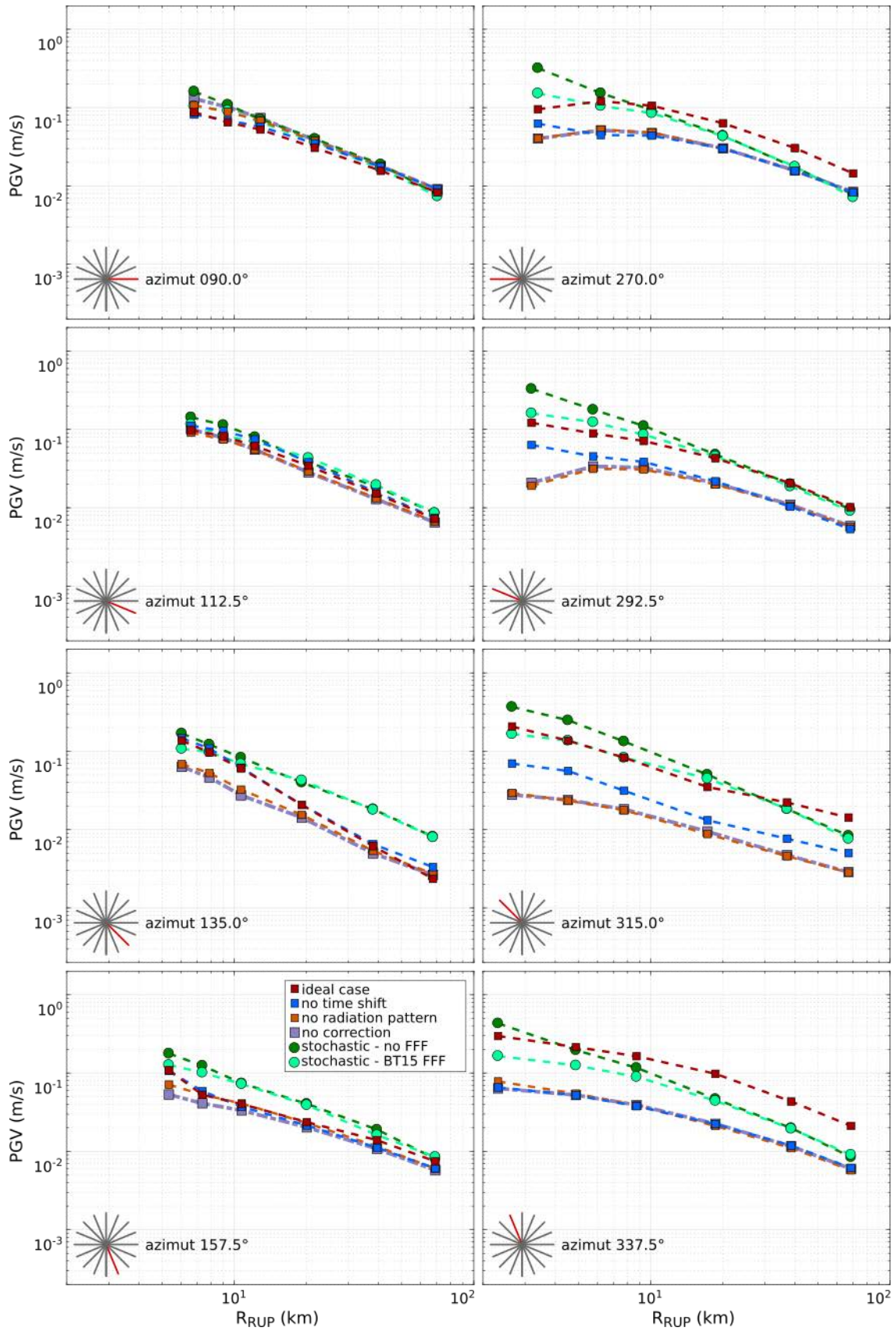


Figure 7 (continued) : Azimuths from 90° to 157.5°N (left) and 270° to 337.5°N (right).

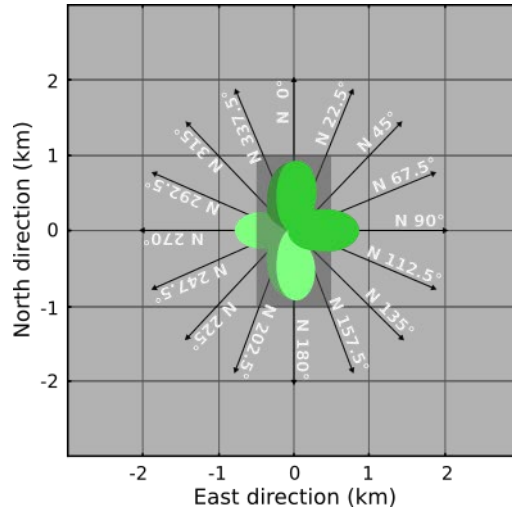


Figure 8: Top view of the S-wave radiation pattern. The radiation pattern is computed for a strike of 0°, 60° of dip, and 0° of rake. The fault plane is represented by a gray rectangle. Only the upper part of the radiation pattern is represented (values for which the energy is radiated towards the surface).

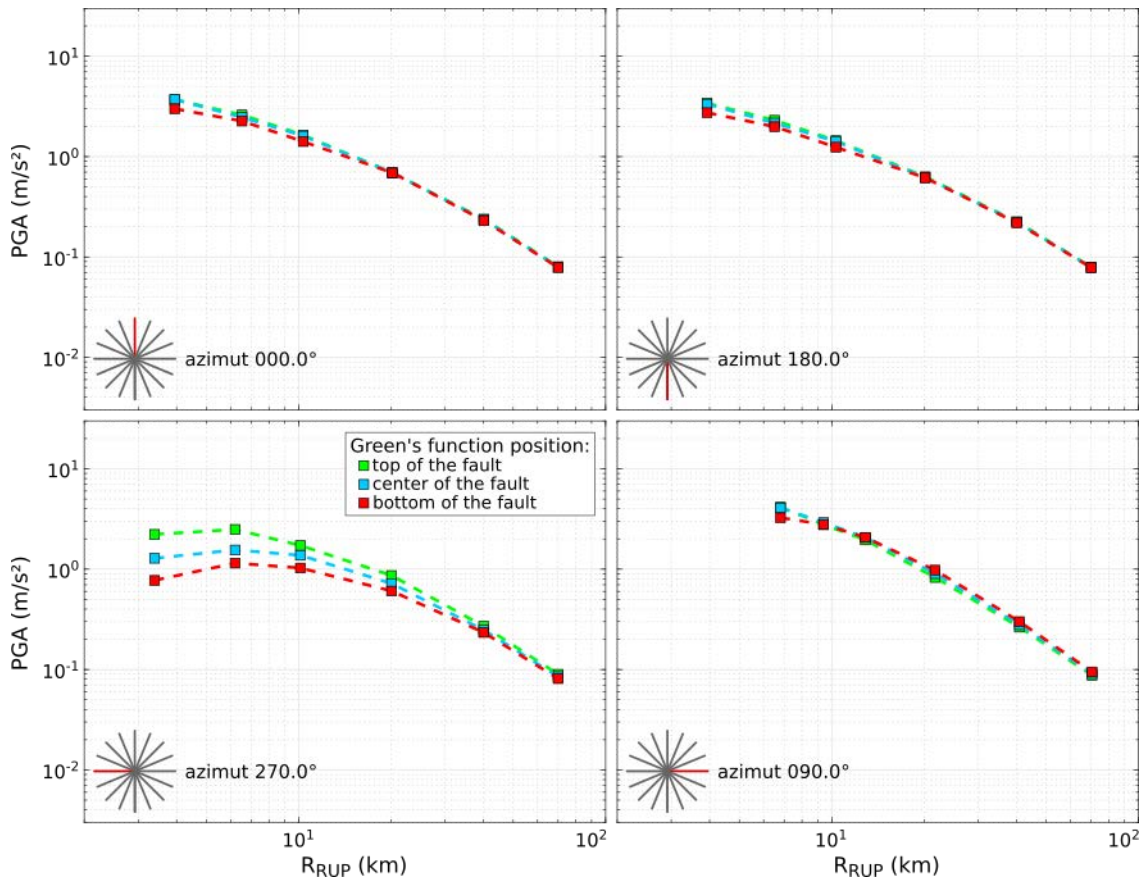


Figure 9: Comparison of acceleration peak values (PGA) calculated with a unique Green's function. Three cases are represented, the unique Green's function is located at the top, at the center and at the bottom of the rupture area.

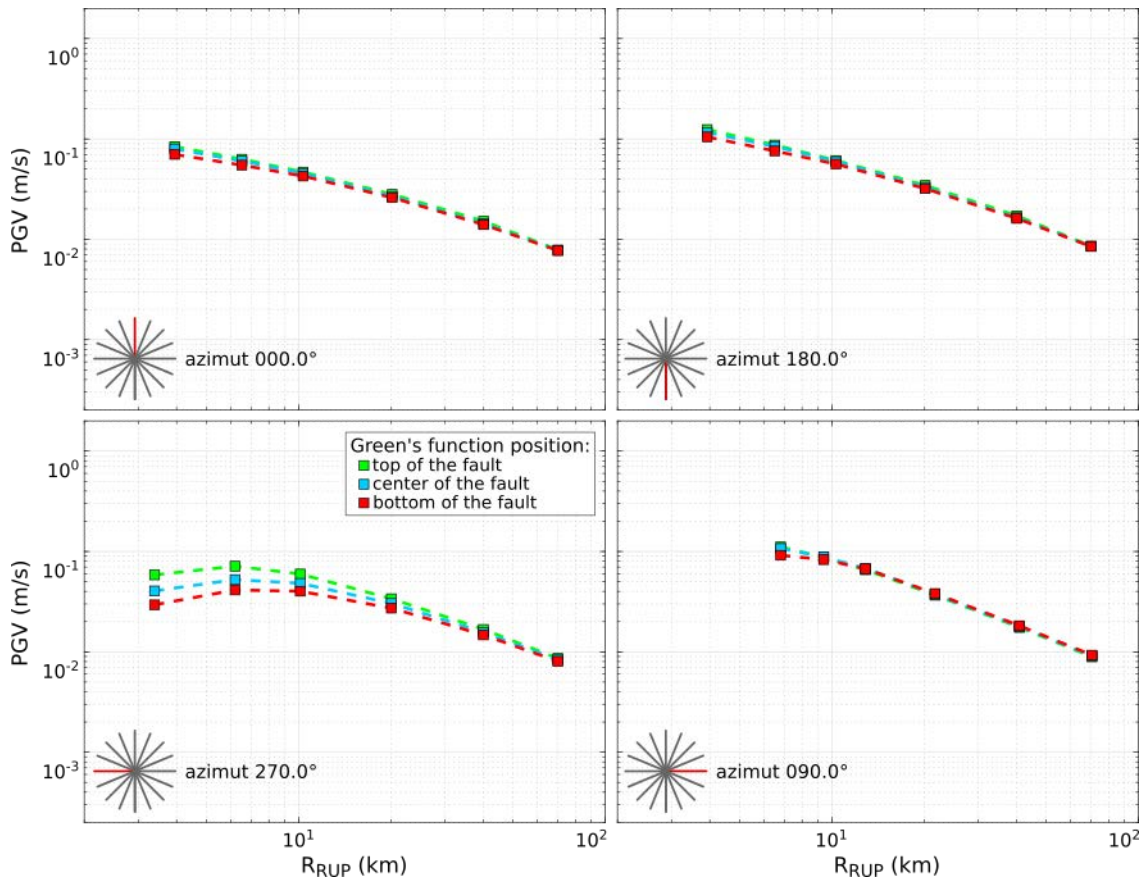


Figure 10: Same as Figure 9 for PGV values.

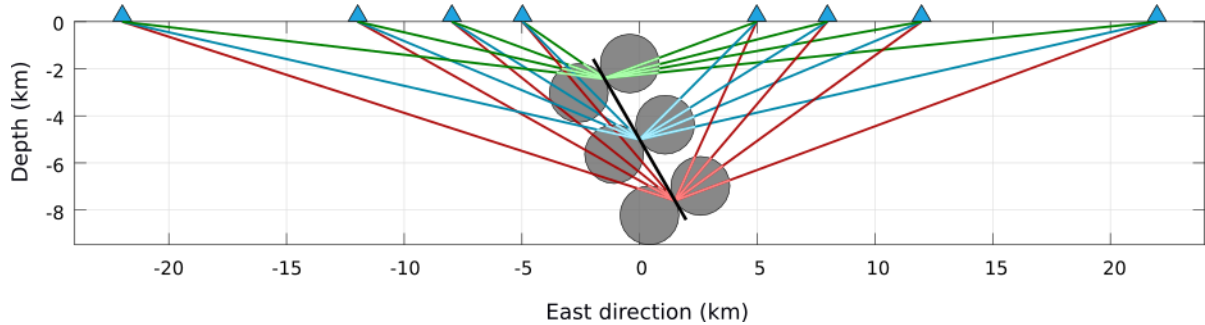


Figure 11: Representation of the S-wave radiation pattern of the 3 Green's functions used for the additional simulations. The stations are represented by triangles. Ray path between the 3 Green's functions (GF) are represented in solid color lines (green for the top GF, blue for the center GF, and red for the bottom GF). The lights colors on the radiation pattern schematically represent the radiation pattern factor.